Table 1. Crystallographic data and refinement statistics. A total of 1663 parameters were refined against 698 restraints and 8765 data to give wR(F^2) = 0.2464 and S = 1.1 (where S is goodness of fit) for weights of $w = 1/[\sigma^2(F^2) + (0.1600P)^2 + 130.00P]$, where $P = ([F^2_{obs} - F^2_{cal}])/3$. The final R factor, R(F), was 0.0824 for the 7025 observed, [$F > 4\sigma$ (F)], data. The largest shift/standard uncertainty was 0.012 in the final refinement cycle. The final difference map had maxima and minima of 0.624 and −0.393 e/Å^3, respectively. Parentheses denote the highest resolution shell. $R_{sym} = \Sigma[\Sigma|F^2_{obs} - F^2_{cal}|]/\Sigma(\Sigma F^2_{obs})/n]$ and R factor $= \Sigma||F_{obs}| - |F_{cal}||/\Sigma|F_{obs}|$, $F_{obs} > 0$.

$(C_{44}H_{54}CuN_{12}O_{15}S_5) \cdot 10.5(H_2O)$	
Formula weight	1404
Molecular weight $(C_{44}H_{54}CuN_{12}O_{15}S_5)$	1217.2
Data collection	
Wavelength	0.71073 Å
Reflections collected	66,370
Refinement	
Redundancy	7.55
I/σ	18.23 (14.81)
Rsym (%)	8.05 (37.62)
Resolution (Å)	1.15
R factor	0.0832
Completeness	99.8
Goodness of fit on F^2	1.1

complex is internalized to the cell, possibly to be associated with pMMO (*5*, *7*, *24*). Further, its metal-ion shuttling role is suggested by structural similarities to the amino acid–containing pyoverdin class of iron siderophores, which also have antibacterial properties (*33*–*36*). In fact, the similarities between methanobactin and the pyoverdin siderophores (e.g., azotobactin and pseudobactin produced by *Azotobacter* spp. and *Pseudomonas* spp.) led to the renaming of CBC to methanobactin.

If methanobactin is indeed a "copper-siderophore" or a "chalkophore" (after the Greek for copper), a specialized copper-trafficking or defense mechanism probably exists in organisms that produce the compound. However, whether methanobactin acts exclusively as an extracellular copper-sequestering agent or has other in vivo functions related to the delivery and insertion of copper ions to copper-containing proteins like pMMO must still be determined. Regardless, the elucidation of the methanobactin structure has major implications in understanding the molecular mechanism of biological methane oxidation and methane cycling in the environment and may also lead to the identification of other copper-trafficking molecules.

References and Notes

1. D. L. Huffman, T. V. O'Halloran, *Annu. Rev. Biochem.* **70**, 677 (2001).
2. L. A. Finney, T. V. O'Halloran, *Science* **300**, 931 (2003).
3. C. Rensing, G. Grass, *FEMS Microbiol. Rev.* **27**, 197 (2003).
4. A. C. Rosenzweig, *Chem. Biol.* **9**, 673 (2002).
5. D. W. Choi *et al.*, *J. Bacteriol.* **185**, 5755 (2003).
6. H.-N. Nguyen *et al.*, *J. Biol. Chem.* **269**, 14995 (1994).
7. J. A. Zahn, A. A. DiSpirito, *J. Bacteriol.* **178**, 1018 (1996).
8. H. Dalton, S. D. Prior, D. J. Leak, S. H. Stanley, in *Microbial Growth on C_1 Compounds*, R. L. C. Hanson, R. S. Hanson, Eds. (American Society for Microbiology, Washington, DC, 1984), pp. 75–82.
9. S. D. Prior, H. Dalton, *J. Gen. Microbiol.* **131**, 155 (1985).
10. S. Lontoh, J. D. Semrau, *Appl. Environ. Microbiol.* **64**, 1106 (1998).
11. J. A. Zahn, D. J. Bergmann, J. M. Boyd, R. C. Kuitz, A. A. DiSpirito, *J. Bacteriol.* **183**, 6832 (2001).
12. S. Tate, H. Dalton, *Microbiology* **145**, 159 (1999).
13. J. A. Vorholt, L. Chistoserdova, S. M. Stolyar, R. K. Thauer, M. E. Lidstrom, *J. Bacteriol.* **181**, 5750 (1999).
14. C. A. Brantner *et al.*, *Can. J. Microbiol.* **43**, 672 (1997).
15. P. Peltola, P. Priha, S. Laakso, *Arch. Microbiol.* **159**, 521 (1993).
16. O. Berson, M. E. Lidstrom, *Environ. Sci. Technol.* **30**, 802 (1998).
17. H. J. Kim, D. W. Graham, *FEMS Microbiol. Lett.* **201**, 133 (2001).
18. G. P. Stafford, J. Scanlan, I. R. McDonald, J. C. Murrell, *Microbiology* **149**, 1771 (2003).
19. O. A. Karlsen *et al.*, *Appl. Environ. Microbiol.* **69**, 2386 (2003).
20. A. A. DiSpirito *et al.*, *J. Bacteriol.* **180**, 3606 (1998).
21. M. W. Fitch *et al.*, *Appl. Environ. Microbiol.* **59**, 2771 (1993).
22. C. M. Tellez, K. P. Gaus, D. W. Graham, R. G. Arnold, R. Z. Guzman, *Appl. Environ. Microbiol.* **64**, 1115 (1998).
23. H. J. Kim, thesis, University of Kansas (2003).
24. H. J. Kim *et al.*, in preparation.
25. Materials and methods are available as supporting material on *Science* Online.
26. G. D. Claycomb, P. M. A. Sherwood, *J. Vac. Sci. Technol. A* **20**, 1230 (2002).
27. S. Puig, E. M. Rees, D. J. Thiele, *Structure* **10**, 1292 (2002).
28. G. M. Sheldrick, SHELXTL version 5 reference manual (Bruker-AXS, Madison, WI), (1994).
29. C. Brückner, S. J. Rettig, D. Dolphin, *Inorg. Chem.* **39**, 6100 (2000).
30. A. A. DiSpirito *et al.*, U.S. Provisional Patent Application Serial No. 60/434, 873 (2004).
31. C. Brükner *et al.*, *Inorg. Chem.* **39**, 6100 (2000).
32. W. Grabarse *et al.*, *J. Mol. Biol.* **303**, 329 (2000).
33. T. Selmer *et al.*, *J. Biol. Chem.* **275**, 3755 (2000).
34. O. Knosp *et al.*, *J. Bacteriol.* **159**, 341 (1984).
35. P. A. Demange *et al.*, *Biochemistry* **27**, 2745 (1988).
36. P. A. Demange *et al.*, *Biochemistry* **29**, 11041 (1990).

37. We thank J. Aube, B. Blagg, K. Camarda, D.W. Choi, T. Ebihara, A. Hooper, B. Elmore, E. Schönbrunn, and T. Williams for assistance on the project. The work was supported by NSF grant no. BES-9407286 (D.W.G.), Department of Energy grant no. 029ER2037 (A.A.D.), and University of Kansas Research Development Funds (D.W.G., C.K.L., M.A.A.). All crystallography was performed at the University of Kansas Crystallography Facility, with the diffractometer provided by NSF grant no. CHE-0079282. The crystal structure of methanobactin has been deposited at the Cambridge Crystallographic Data Centre and allocated the deposition number CCDC 241254. This work was done in fulfillment of dissertation requirements of H.J.K. at the University of Kansas, Department of Civil, Environmental, and Architectural Engineering.

Supporting Online Material

www.sciencemag.org/cgi/content/full/305/5690/1612/DC1
Materials and Methods
Figs. S1 and S2

25 March 2004; accepted 3 August 2004

Activation of Endogenous Cdc42 Visualized in Living Cells

Perihan Nalbant,* Louis Hodgson,* Vadim Kraynov, Alexei Toutchkine, Klaus M. Hahn†

Signaling proteins are tightly regulated spatially and temporally to perform multiple functions. For Cdc42 and other guanosine triphosphatases, the subcellular location of activation is a critical determinant of cell behavior. However, current approaches are limited in their ability to examine the dynamics of Cdc42 activity in living cells. We report the development of a biosensor capable of visualizing the changing activation of endogenous, unlabeled Cdc42 in living cells. With the use of a dye that reports protein interactions, the biosensor revealed localized activation in the trans-Golgi apparatus, microtubule-dependent Cdc42 activation at the cell periphery, and activation kinetics precisely coordinated with cell extension and retraction.

Cdc42, a member of the Rho family of small guanosine triphosphatase (GTPase) proteins, regulates multiple cell functions, including motility, proliferation, apoptosis, and cell morphology (*1*–*3*). In order to fulfill these diverse roles, the timing and location of Cdc42 activation must be tightly controlled. The Cdc42 biosensor used here to examine the spatiotemporal dynamics of Cdc42 activation represents an in vivo application of a dye (I-SO) designed specifically to report protein conformational changes and protein interactions in living cells (*4*). In this biosensor, a domain from the Cdc42 effector protein WASP that binds only to activated Cdc42 was covalently labeled with the dye. The labeled domain showed a strong increase in fluorescence intensity upon binding to activated, underivatized Cdc42.

On the basis of the nuclear magnetic resonance (NMR) structure of the Cdc42-WASP

Department of Pharmacology, University of North Carolina School of Medicine, Chapel Hill, NC 27599–7365, USA.

*These authors contributed equally to this work.
†To whom correspondence should be addressed. E-mail: khahn@med.unc.edu

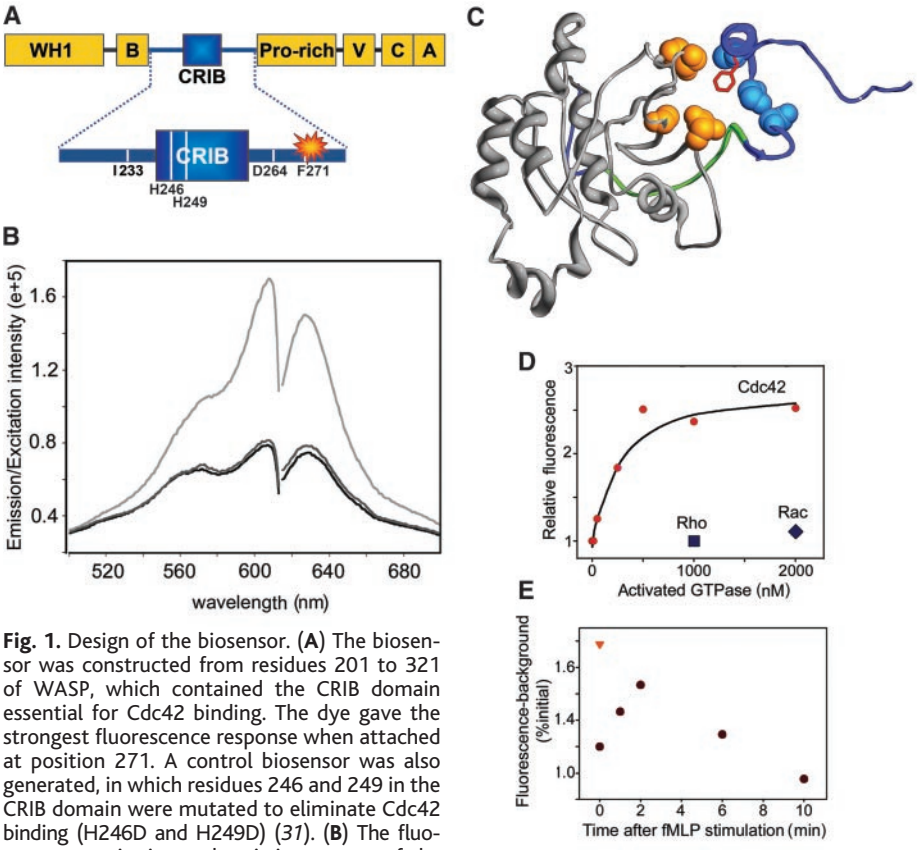

Fig. 1. Design of the biosensor. (**A**) The biosensor was constructed from residues 201 to 321 of WASP, which contained the CRIB domain essential for Cdc42 binding. The dye gave the strongest fluorescence response when attached at position 271. A control biosensor was also generated, in which residues 246 and 249 in the CRIB domain were mutated to eliminate Cdc42 binding (H246D and H249D) (*31*). (**B**) The fluorescence excitation and emission spectra of the biosensor showed a 2.8-fold increase in intensity upon interacting with activated Cdc42 (black line, biosensor alone; dark gray line, biosensor with saturating Cdc42-GDP; light gray line, biosensor with saturating Cdc42-GTPγS). (**C**) Binding of the biosensor to Cdc42 placed the dye attached at position 271 (red) in a hydrophobic pocket formed by amino acids from both WASP (blue) and Cdc42 (orange). The CRIB domain is shown in green. (**D**) The biosensor showed a concentration-dependent fluorescence increase in response to Cdc42-GTPγS, but did not respond to Rho-GTPγS or Rac-GTPγS. (**E**) Human neutrophils were lysed at different times after stimulation with fMLP, and biosensor was added to the lysates. Circles, fluorescence intensity in lysates at each time point; triangle, unstimulated lysate equilibrated with GTPγS.

complex (*5*), the dye was tested at three positions (I233, D264, and F271 of WASP) to optimize fluorescence response and binding (Fig. 1A). Site-specific labeling was accomplished by inserting a single cysteine and reacting the WASP domain with cysteine-selective iodoacetamide dye (*4*). The dye showed the greatest response at position 271, undergoing a 2.8-fold increase in fluorescence intensity upon binding to Cdc42-GTPγS, relative to either biosensor alone or GDP-loaded Cdc42 (Fig. 1B). The NMR structure of the Cdc42-WASP complex indicated that the dye at position 271 is inserted into a hydrophobic pocket formed from amino acids of both Cdc42 and WASP (Fig. 1C). The dissociation constant (K_d) for the Cdc42-biosensor interaction, determined by fitting fluorescence changes to the Michaelis equation, was 150 ± 50 nM (Fig. 1D). This was slightly higher than previously reported for a similar, unlabeled WASP fragment (77 ± 9 nM) (*6*), indicating that the dye minimally perturbed binding of the domain. To determine the specificity of the biosensor, we examined interactions with different activated GTPases. The biosensor distinguished proteins closely related to Cdc42 from other members of the Rho family. It did not interact with RhoA or Rac at concentrations well above physiological levels (Fig. 1D), but responded to both Cdc42 and the closely related protein TC10, which bind WASP with similar affinity (*7*) (fig. S1).

Figure 1E shows that the labeled WASP fragment provides a straightforward means to assay Cdc42 activation in cell lysates. By simply adding the biosensor to the lysate, one can obtain a fluorescence readout of Cdc42 activa-

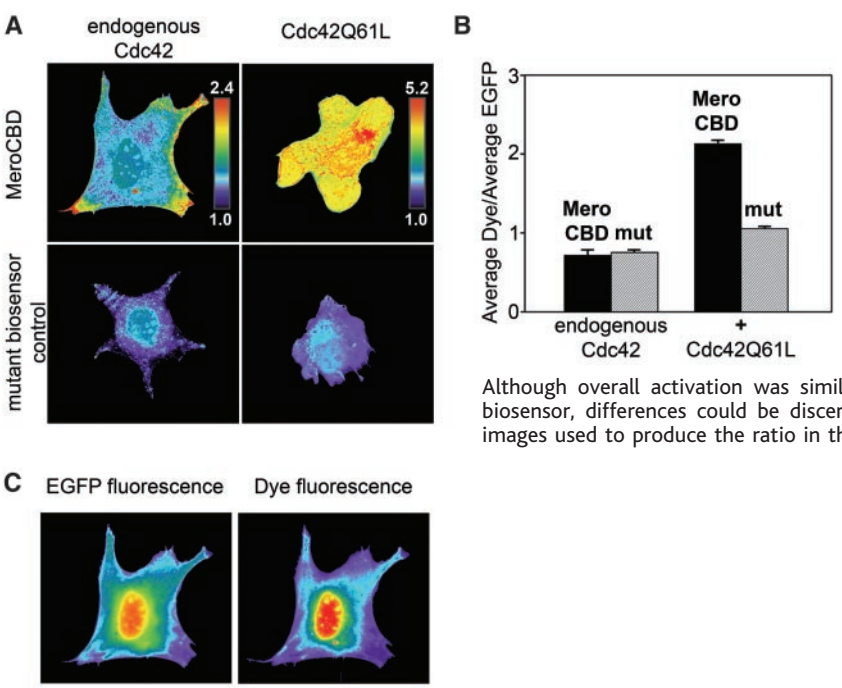

Fig. 2. Activation of endogenous Cdc42 in living cells. (**A**) Distribution of activated Cdc42 in MEF/3T3 cells. Cells were injected with MeroCBD (upper panels) or with mutant control biosensor (lower panels). MeroCBD showed localized activation of endogenous, wild-type Cdc42 in unstimulated cells (left column). Overexpression of constitutively active Cdc42-Q61L (right column) led to increased activation signal throughout the cell. Results were unaffected by biosensor concentrations over the broad range examined (EGFP fluorescence per unit area = 50 to 400, normalized for exposure time). (**B**) Average Cdc42 activity in cells with and without expression of Cdc42-Q61L (with Cdc42-Q61L = mean ± SEM: 12 MeroCBD cells, 7 control cells; without Cdc42-Q61L = mean ± SEM: 7 MeroCBD cells, 11 control cells). Although overall activation was similar in unstimulated cells loaded with real versus control biosensor, differences could be discerned because activation was localized. (**C**) EGFP and dye images used to produce the ratio in the cell shown at upper left in (A).

tion. The method was used to determine the kinetics of Cdc42 activation in neutrophils after stimulation with chemoattractant fMetLeuphe (fMLP) peptide. Results paralleled those previously reported using well-established methods (*8*). Fluorescence of the biosensor was also used to monitor the real-time kinetics of Cdc42 GDP/GTP exchange in vitro (fig. S2D).

Because the labeled WASP fragment responded to activated Cdc42 through fluorescence intensity modulation, a ratiometric imaging approach was used to correct for effects of varying cell thickness, uneven illumination, and other factors that could affect imaging of dye intensity (*9*). The biosensor was fused to enhanced green fluorescent protein (EGFP) to provide a fluorescence signal insensitive to Cdc42 binding, but with the same subcellular distribution as the sensitive dye. The dye image could be divided by the EGFP image to normalize changes in dye intensity not originating from Cdc42 binding. A proline-rich region of WASP (amino acids 315 to 321) was also deleted to preclude possible binding to proteins containing SH3 domains. Fluorescence response and Cdc42 binding of the biosensor remained intact after these modifications (fig. S2A). It was named MeroCBD, for the combination of the Cdc42 binding domain with a merocyanine dye.

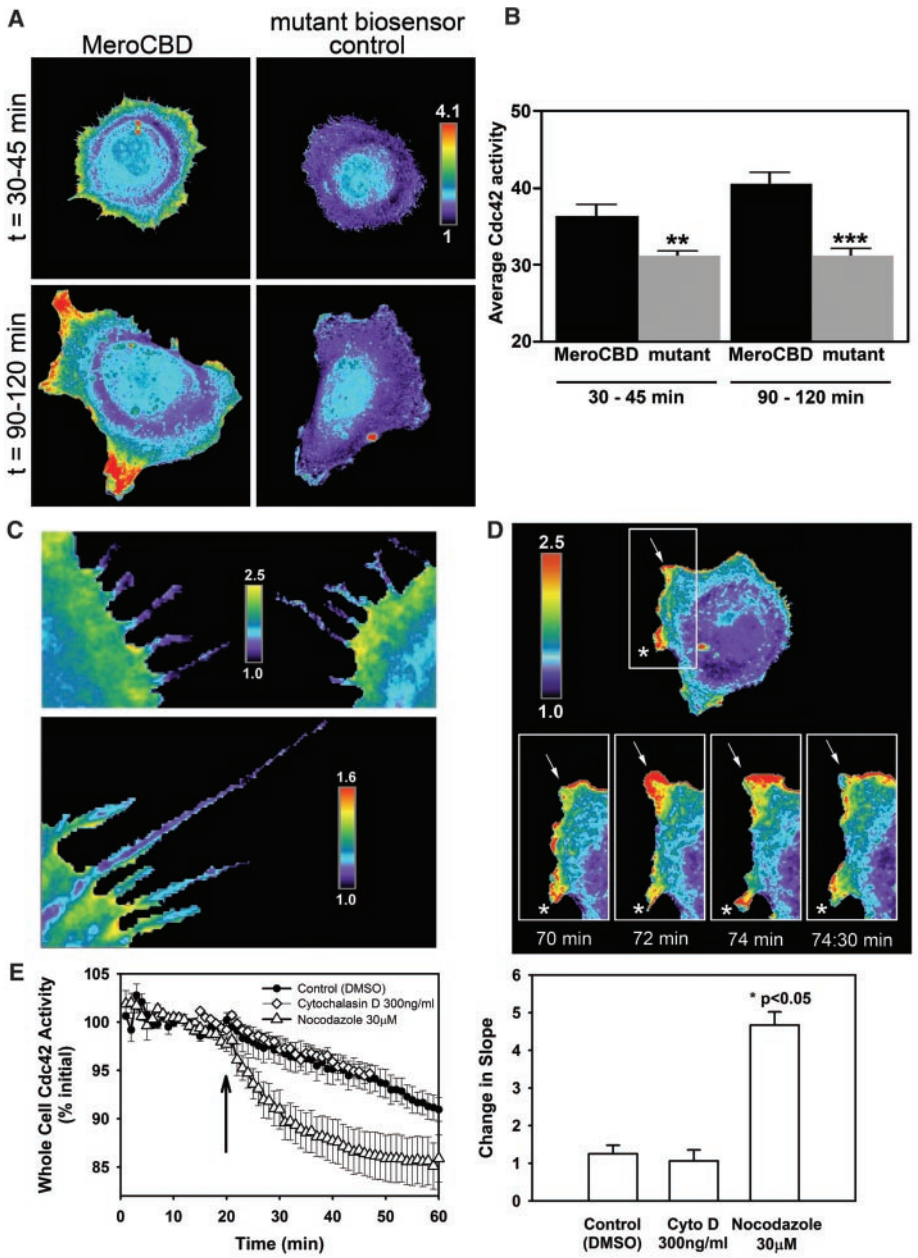

Fig. 3. Cdc42 activation during cell adhesion and spreading. (**A**) Cdc42 activation was examined at different times after MEF/3T3 cell adhesion to fibronectin. Activity was first distributed in a narrow band around the cell, then concentrated in the larger protrusions that formed at later time points (n = 11 cells at 30 to 45 min, n = 22 cells at 90 to 120 min). (**B**) Total integrated Cdc42 activity divided by cell area (average cellular activation) was higher during later stages when cells were polarized and producing large extensions (t = 30 to 45 min: $^{**}P < 0.01$, n = 11 cells; t = 90 to 120 min: $^{***}P < 0.001$, n = 12 cells). Error bars represent the SEM. (**C**) Activation was observed at the cell edges near filopodia, but not in the filopodia themselves (n > 300 filopodia). Areas of low activation sometimes extended into the cell at the base of filopodia (lower panel). (**D**) Active remodeling of the cell perimeter was associated with high levels of Cdc42 activation (movies S1 to S3). (**E**) Cells were treated with nocodazole (30 μM, n = 7 cells), cytochalasin D (300 ng/ml, n = 9 cells), or dimethyl sulfoxide (DMSO) control (n = 6 cells). Average whole-cell Cdc42 activity was monitored before and after drug treatment (at the time indicated by the arrow). Error bars represent the SEM. See movies S4 to S6.

The biosensor was injected into living fibroblasts, where it showed localized Cdc42 activation even in unstimulated cells, which was highest at cell extensions (Fig. 2A). In cells expressing constitutively active Cdc42-Q61L (*10*), the overall levels of activity shown by MeroCBD were much higher (Fig. 2, A and B), and activation was distributed throughout the cell. It was important to show that the dye was not binding nonspecifically to membranes or to other hydrophobic cell components that could produce spurious fluorescence intensity increases. When MeroCBD was compared to a control biosensor with severely reduced Cdc42 binding (Fig. 2B; fig. S2, B and C), the mutant biosensor showed no localized activation for either endogenous or dominant positive Cdc42 (Fig. 2A), and showed only slightly increased total activity in cells expressing Cdc42-Q61L (Fig. 2B). Simple localization of the CBD-EGFP was not sufficient to reveal Cdc42 activation (Fig. 2C).

The ability to detect endogenous protein with the high sensitivity provided by the dye was important in studying Cdc42. High sensitivity enabled detection of protein activation at native concentrations, unlike previous fluorescence resonance energy transfer (FRET) biosensors that required overexpression of Cdc42 (*11*), and showed more uniform activation. MeroCBD did not require modification of the Cdc42 terminus with a GFP mutant for FRET (*12*), thus maintaining normal regulation by guanosine dissociation inhibitors (GDIs) (*13*).

Cdc42 is known to be important for maintaining cell polarity in motility (*14*), but the role of localized Cdc42 activation is poorly understood. Cdc42 promotes leading-edge extension through activation of Rac and of WASP, which causes Arp2/3 to nucleate actin filaments (*15*, *16*). It also induces the fine cell extensions known as filopodia (*17*, *18*). The relative spatiotemporal dynamics of Cdc42 activation, protrusion, and filopodia formation were examined in fibroblasts as they attached and spread on fibronectin (*19*). At 30 to 45 min after plating, Cdc42 was

activated in a thin band at cell edges extending filopodia (Fig. 3A). No activation was observed within the filopodia themselves (Fig. 3C). Regions of lower activation sometimes extended into the cell body at the base of filopodia (Fig. 3C, lower cell), consistent with studies showing that actin bundles in filopodia extend into the cell body (*20*). At 90 to 120 min after attachment, activity became localized within larger dynamic protrusions, and overall activity increased (Fig. 3B); protrusions had more than twice the average activity of any other region (n = 22 cells) (Fig. 3, A and D) (movies S1 to S3; see also motion control fig. S6). Controls showed that biosensor levels did not perturb spreading or motility (figs. S3 to S5).

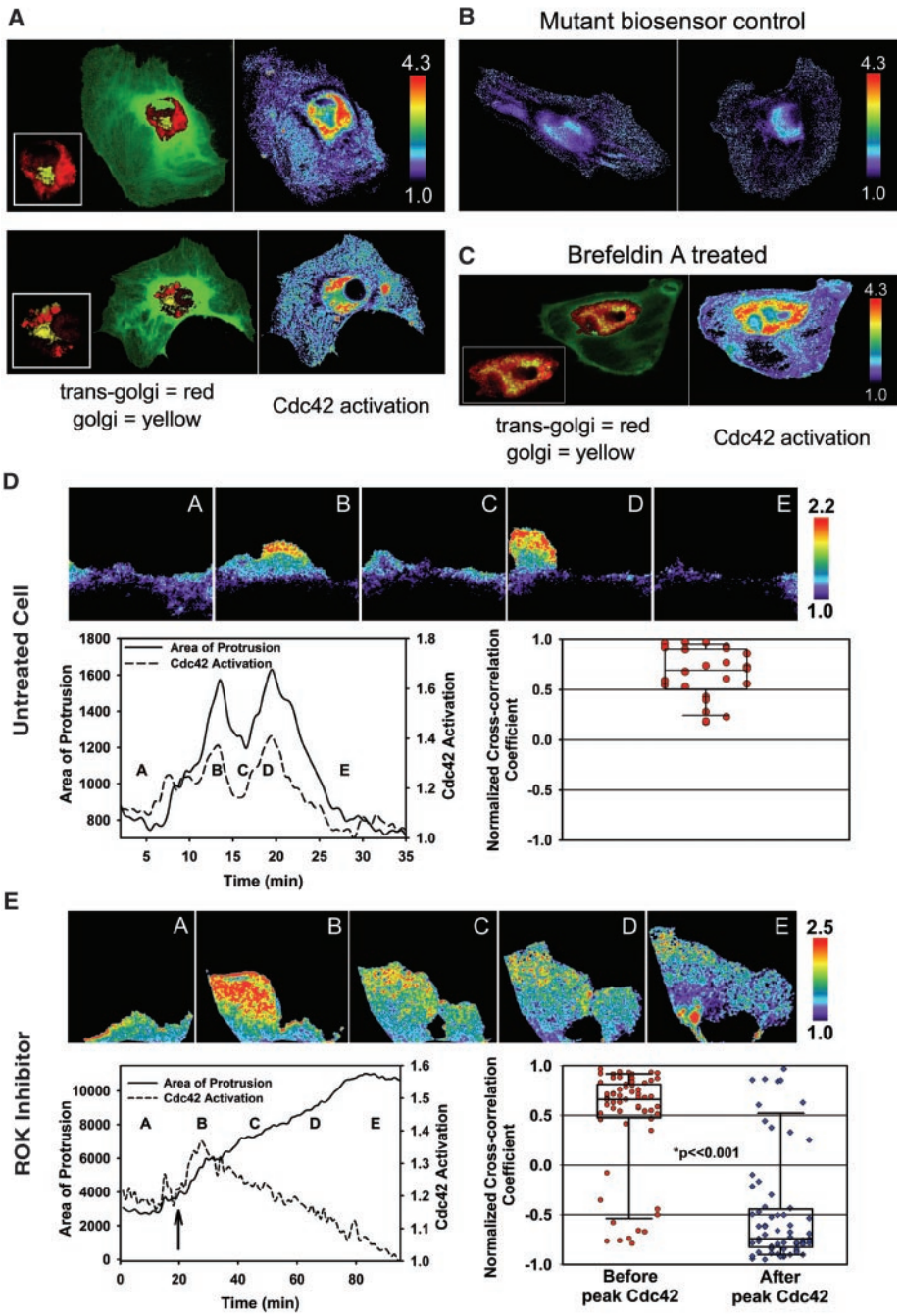

Fig. 4. Cdc42 activation at trans-Golgi. Activation kinetics synchronized with extension and retraction. (**A**) Immunofluorescence colocalization of trans-Golgi markers and Cdc42 activation in human umbilical vein–derived endothelial cells (HUVEC). Trans-Golgi fluorescence is in red, Golgi fluorescence is in yellow. EGFP fluorescence is in green. (**B**) Mutant control biosensor in fixed HUVEC cells. (**C**) Upon collapsing the Golgi using Brefeldin A, the trans-Golgi and Cdc42 activation remained intact. (**D**) For individual protrusions, area and Cdc42 activation per unit area were monitored over time. Of 22 cell regions analyzed, 17 showed high synchrony between protrusions and Cdc42 activity during both extension and retraction, as was apparent through inspection of the graphs and using cross-correlation analysis (*32*). Data from a representative protrusion are shown. Images correspond to the time points indicated in the plots. All other data are shown in fig. S7. (**E**) When cells were treated with Rho kinase inhibitor Y27632 (30 μM, at the time indicated by the arrow), cells continued to extend even after Cdc42 activation receded (see also fig. S8 and movie S7).

Microtubules or actin may direct Cdc42 activation to specific peripheral locations (*21*–*24*). We explored this possibility by treating cells with the microtubule-depolymerizing agents nocodazole and colchicine, or with cytochalasin D, an inhibitor of actin polymerization. Only nocodazole and colchicine markedly affected peripheral Cdc42 activation (Fig. 3E; fig. S9, movies S4 to S6). Microtubules may localize interactions between Cdc42 and guanine nucleotide exchange factors (*25*), by directing vesicle trafficking or regulating events at adhesion complexes (*26*, *27*). Cdc42 has been implicated in intracellular trafficking (*28*–*30*). Our biosensor consistently showed activation in the trans-Golgi apparatus of endothelial cells (Fig. 4, A to C), and sometimes also in fibroblasts. Activation in this major secretory compartment suggests that Cdc42 regulates directional sorting or trafficking of polarity cues, or that microtubules mediate trafficking of activated Cdc42 to specific portions of the periphery (Fig. 3E).

Using the dye's ability to obtain more than a hundred sequential images at low biosensor concentrations, we carried out high-resolution kinetic studies of Cdc42 activation during extension and retraction of individual protrusions (Fig. 4D; fig. S7). Using an algorithm to objectively determine the boundaries of protrusions, we plotted the changing areas of individual protrusions against the protrusions' total activation per unit area. The rise and fall of Cdc42 activity was markedly correlated with both extension and retraction. This close correlation suggested that Cdc42 activation and deactivation could be rate-determining steps for extension and retraction. Alternatively, upstream signals might coordinately inhibit Cdc42 activity while inducing retraction. We distinguished these possibilities by blocking retraction using an inhibitor of Rho kinase (Y27632). This caused protrusions to continue expanding even after Cdc42 activity decreased (Fig. 4E; fig. S8 and movie S7), indicating that upstream signals (possibly regulated by the microtubule cytoskeleton) control Cdc42 activity and retraction in parallel. Cdc42 activity did not remain elevated during protrusion, suggesting that Cdc42 initiates rather than maintains extension.

MeroCBD exemplifies a biosensor approach that combines the ability to sense endogenous molecules with the sensitivity provided by direct excitation of a fluorescent dye. This extends our ability to examine proteins that cannot be derivatized or overex-

pressed for live cell studies, and enabled detailed kinetic analysis of rapid cellular processes. The biosensor revealed Cdc42 activation in the trans-Golgi compartment, microtubule-dependent activation at the cell periphery but not in filopodia, and tightly coordinated kinetics of cell extension, retraction, and Cdc42 activation.

References and Notes

1. J. W. Erickson, R. A. Cerione, *Curr. Opin. Cell Biol.* **13**, 153 (2001).
2. L. Kjoller, A. Hall, *Exp. Cell Res.* **253**, 166 (1999).
3. M. C. Subauste *et al.*, *J. Biol. Chem.* **275**, 9725 (2000).
4. A. Toutchkine, V. Kraynov, K. Hahn, *J. Am. Chem. Soc.* **125**, 4132 (2003).
5. N. Abdul-Manan *et al.*, *Nature* **399**, 379 (1999).
6. M. G. Rudolph *et al.*, *J. Biol. Chem.* **273**, 18067 (1998).
7. E. Vignal *et al.*, *J. Biol. Chem.* **275**, 36457 (2000).
8. V. Benard, B. P. Bohl, G. M. Bokoch, *J. Biol. Chem.* **274**, 13198 (1999).
9. G. R. Bright, G. W. Fisher, J. Rogowska, D. L. Taylor, *Methods Cell Biol.* **30**, 157 (1989).
10. P. J. Miller, D. I. Johnson, *Mol. Cell. Biol.* **14**, 1075 (1994).
11. A. Seth, T. Otomo, H. L. Yin, M. K. Rosen, *Biochemistry* **42**, 3997 (2003).
12. R. E. Itoh *et al.*, *Mol. Cell. Biol.* **22**, 6582 (2002).
13. G. R. Hoffman, N. Nassar, R. A. Cerione, F. Bachmair, *Cell* **100**, 345 (2000).
14. S. Etienne-Manneville, *J. Cell Sci.* **117**, 1291 (2004).
15. A. L. Bishop, A. Hall, *Biochem. J.* **348**, 241 (2000).
16. H. N. Higgs, T. D. Pollard, *J. Cell Biol.* **150**, 1311 (2000).
17. C. D. Nobes, A. Hall, *Biochem. Soc. Trans.* **23**, 456 (1995).
18. R. Kozma, S. Ahmed, A. Best, L. Lim, *Mol. Cell. Biol.* **15**, 1942 (1995).
19. L. S. Price, J. Leng, M. A. Schwartz, G. M. Bokoch, *Mol. Biol. Cell* **9**, 1863 (1998).
20. T. M. Svitkina *et al.*, *J. Cell Biol.* **160**, 409 (2003).
21. S. Etienne-Manneville, A. Hall, *Cell* **106**, 489 (2001).
22. C. M. Waterman-Storer, R. A. Worthylake, B. P. Liu, K. Burridge, E. D. Salmon, *Nat. Cell Biol.* **1**, 45 (1999).
23. C. Higashida *et al.*, *Science* **303**, 2007 (2004).
24. R. Wedlich-Soldner, S. Altschuler, L. Wu, R. Li, *Science* **299**, 1231 (2003).
25. A. Schmidt, A. Hall, *Genes Dev.* **16**, 1587 (2002).
26. I. R. Nabi, *J. Cell Sci.* **112**, 1803 (1999).
27. A. F. Palazzo, G. G. Gundersen, *Sci. STKE* **2002**, pe31 (2002).
28. J. W. Erickson, C. Zhang, R. A. Kahn, T. Evans, R. A. Cerione, *J. Biol. Chem.* **271**, 26850 (1996).
29. W. J. Wu, J. W. Erickson, R. Lin, R. A. Cerione, *Nature* **405**, 800 (2000).
30. R. A. Cerione, *Trends Cell Biol.* **14**, 127 (2004).
31. H. Miki, T. Sasaki, Y. Takai, T. Takenawa, *Nature* **391**, 93 (1998).
32. J. T. Mandeville, R. N. Ghosh, F. R. Maxfield, *Biophys. J.* **68**, 1207 (1995).

33. We are grateful to P. Hordijk, G. Bokoch, and L. Dehmelt for critical reading of the manuscript; to G. Bokoch for help with neutrophil stimulation assays; and to M. Berba for secretarial assistance. This work was funded by grants from the Deutsche Forschungsgemeinschaft (P.N.), the Arthritis Foundation (V.K.), the Leukemia and Lymphoma Society (A.T.), and by the NIH (grants GM57464 and GM64346) (K.M.H.). K.M.H. has a financial interest in and is a consultant for and member of the Scientific Advisory Board for Genospectra Company, which seeks to develop products that precisely characterize molecular events that occur in cells.

Supporting Online Material

www.sciencemag.org/cgi/content/full/305/5690/1615/DC1
Materials and Methods
Figs. S1 to S9
Movies S1 to S7
References

17 May 2004; accepted 30 July 2004

Advanced Cardiac Morphogenesis Does Not Require Heart Tube Fusion

Shanru Li,[1] Deying Zhou,[1] Min Min Lu,[1] Edward E. Morrisey[1,2]*

The bilateral cardiac mesoderm migrates from the lateral region of the embryo to the ventral midline, where it fuses to form the primitive heart tube. It is generally accepted that migration and fusion are essential for subsequent stages of cardiac morphogenesis. We present evidence that, in *Foxp4* mutant embryonic mice, each bilateral heart-forming region is capable of developing into a highly differentiated four-chambered mammalian heart in the absence of midline fusion. These data demonstrate that left-right chamber specification, cardiac looping, septation, cardiac myocyte differentiation, and endocardial cushion formation are preprogrammed in the precardiac mesoderm and do not require midline positional identity or heart tube fusion.

Although the molecular mechanisms underlying cardiac myocyte differentiation have been extensively examined and initial molecular pathways have been identified, much less is understood about how specified myocardial cells form the primitive heart tube and the four-chambered mammalian heart. This complex morphological process has a major impact on human health, because cardiovascular defects account for a substantial percentage of neonatal congenital disease. The bilateral precardiac mesoderm forms at the anterior pole of the vertebrate embryo (*1*, *2*). How this mesoderm migrates to the ventral midline to form the single heart tube in the embryo is not well understood, although contributions from anterior foregut endoderm have been implicated. Moreover, whether this fusion event is required for cardiac differentiation and morphogenesis is not known, although some markers of the cardiac myocyte lineage that become spatially restricted in later development (such as *eHAND*, *MLC2a*, and *MLC2v*) are expressed throughout the early precardiac mesoderm (*1*, *2*). The heart is also the first organ to exhibit left-right asymmetry. Whether this asymmetry is preprogrammed into the precardiac mesoderm or whether it is acquired coincident with midline fusion is unknown. Most genetic models of defective heart tube fusion, also known as cardia bifida, are characterized by bilateral regions of specified cardiac mesoderm that express cardiac-specific genes but fail to progress through later stages of cardiac morphogenesis (*3*–*5*). In addition, most murine models of cardia bifida exhibit additional extracardiac defects in body pattern formation, including severe defects in ventral morphogenesis and embryonic turning (*3*, *6*). These data have led to a working model in which ventral midline fusion of the bilateral cardiac primordia is essential for subsequent cardiac development and morphogenesis, especially later aspects of chamber identity, left-right cardiac asymmetry, and looping morphogenesis (*1*, *7*).

We have previously cloned and characterized *Foxp4*, a member of the Fox gene family that is expressed in multiple tissues, including the lung, gut, and brain, in the developing mouse embryo (*8*, *9*). *Foxp4* is expressed in early foregut endoderm and later in development in lung and hindgut (*8*). To generate a mutant allele of *Foxp4*, we replaced two exons encoding the forkhead DNA binding domain with the neomycin resistance cassette (fig. S1, A and B). Proper gene targeting was confirmed by Southern blotting and polymerase chain reaction (fig. S1, D and E). Immunohistochemistry with a Foxp4-specific polyclonal antibody confirmed that mutant embryos no longer expressed Foxp4 protein, suggesting that we had generated a null allele (fig. S1C). Heterozygous embryos were fertile and exhibited no obvious defects (*10*). The majority of homozygous embryos died around embryonic day 12.5 (E12.5) (table S1).

Histological analysis from E8.5 to E12.5 revealed the development of two complete hearts in *Foxp4* mutant embryos (Fig. 1B). This was apparent as early as E8.5, when midline fusion of the bilateral cardiac primordia has normally occurred (Fig. 1, C and D). The two hearts in *Foxp4* mutants were positioned bilaterally, suggesting a lack of proper migration of the precardiac primordia to the midline (Fig. 1, C to H). *Foxp4* mutants exhibited grossly normal ventral morphogenesis and embryonic turning (Fig. 1, A to H), suggesting that cardia bifida was not due to secondary defects in these processes, as has been observed in other mouse models (*3*–*6*, *11*). Upon sacrifice (E8.5 to E12.5), each of the two bilateral hearts was beating at approximately the same rate as in wild-type embryos, although they were asynchronous (*10*).

[1]Department of Medicine, [2]Department of Cell and Developmental Biology, University of Pennsylvania, Philadelphia, PA 19104, USA.

*To whom correspondence should be addressed. E-mail: emorrise@mail.med.upenn.edu